A Data-Driven Verilog-A ReRAM Model

Ioannis Messaris, Alexander Serb, *Member, IEEE,* Spyros Stathopoulos, Ali Khiat,
Spyridon Nikolaidis, *Senior Member, IEEE,* and Themistoklis Prodromakis, *Senior Member, IEEE*

***Abstract*—The translation of emerging application concepts that exploit Resistive Random Access Memory (ReRAM) into large-scale practical systems requires realistic yet computationally efficient device models. Here, we present a ReRAM model where device current-voltage characteristics and resistive switching rate are expressed as a function of a) bias voltage and b) initial resistive state. The model's versatility is validated on detailed characterization data, for both filamentary valence change memory and non-filamentary ReRAM technologies, where device resistance is swept across its operating range using multiple input voltage levels. Furthermore, the proposed model embodies a window function which features a simple mathematical form analytically describing resistive state response under constant bias voltage as extracted from physical device response data. Its Verilog-A implementation captures the ReRAM memory effect without requiring integration of the model state variable, making it suitable for fast and/or large-scale simulations and overall interoperable with current design tools.**

***Index Terms*—Characterization, modeling, ReRAM, simulation, Verilog-A.**

I. Introduction

SINCE 2008 when the basic resistive switching property of a double-layer nano-scale film based on titanium dioxide was studied [1] and linked to Chua's theory of the 'memristor' [2], understanding of practical memristor realizations has moved far beyond the simple 'moving barrier' model. Solid-state memristor devices stem from different technological roots (phase-change memory, spin-torque transfer, metal-oxide etc. [3], [4], [5]) and employ a variety of electrode/active layer materials and geometries. Such devices are becoming more and more accessible to researchers, and it is now more clear on how different implementations feature properties that render them suitable for different applications. There are memristors that have been reported to switch quickly and in a probabilistic fashion [6], while others can have their resistive state (RS) shifted in small continuous steps [7] that are ideal for synaptic learning and reconfigurable electronics [8], [9]. Resistive Random Access Memory (ReRAM) devices are a class of (metal-oxide) memristors that support multi-state programming, can be programmed swiftly and with low energy and can be compatible with post-CMOS processing.

This work was supported in part by the EU COST Action IC1401 MEMOCIS and the Engineering and Physical Sciences Research Council under Grant EP/K017829/1.

The data from this paper can be obtained from University of Southampton e-Prints Repository DOI:xxxx.

I. Messaris and S. Nikolaidis was with the Department of Physics, Aristotle University of Thessaloniki, 54124 Thessaloniki Greece (email: imessa@physics.auth.gr).

A. Serb, S. Stathopoulos, A. Khiat and T. Prodromakis are with the Nano Group, ECS, University of Southampton, Highfield, Southampton SO17 1BJ. (email: A.Serb@soton.ac.uk.)

In general, a 1st order, extended, voltage controlled memristive system is expressed as,

$$i = G(x, v)v \tag{1}$$

$$\frac{dx}{dt} = g(x, v) \tag{2}$$

where, i is the current flowing through the device, v is the voltage applied on its terminals and x is the device's internal state variable. Equation (1) calculates the current flowing through the device as a function of the state variable (x) and bias voltage (v) while function $g(\cdot)$ in (2) describes the dependency of the state variable time-derivative on the same variables (x, v).

Among the well-established, generalized, voltage controlled memristor models published to date, the model presented in [10] uses a linear or exponential relationship for (1), while models [11], [12] and [13] utilize a hyperbolic sinusoidal expression to approximate the Simmons tunneling barrier model which describes the $I-V$ characteristics of metal-insulator-metal (MIM) memristive devices [14]. Regarding equation (2), the mentioned models (besides [13]) have their internal state (x) and external stimuli (v) dependencies expressed by separate functions which are linked orthogonally, i.e. $g(x, v) = s(v) \times f(x)$. Function $s(v)$ expresses the device's '(voltage) switching sensitivity' for which various non-linear forms have been proposed such as the simple exponential presented in [11] or the more complex a-power law function in [10]. Function $f(x)$ corresponds to the 'window function' that bounds the device state variable in a fixed range (projected to a fixed resistive range $[\, R_{min}, R_{max}\,]$) and models the experimentally verified nonlinear kinetics in the state variable motion as it approximates these constant boundaries (maximum and minimum resistive states R_{min}, R_{max}). A number of window functions have been presented ([11], [15], [16], [17]) which take various mathematical forms, though the fitting parameters in these expressions are hard to extract from characterization data which in most cases are particularly noisy.

As different physical models describe different types of ReRAM devices ([18], [19]), here, we present a general, empirical, 1st order, voltage controlled ReRAM model for devices exhibiting non-volatile, bipolar switching characteristics. The state variable of the proposed model is the device RS (R) which can be easily measured with modern characterization instrumentation ([20]) therefore establishing a direct link between experimental data and model parameters. The $I-V$ relationship (1) is proportional to device conductance ($1/R$) and a voltage controlled hyperbolic sinusoid. The 'sensitivity' function $s(v)$ takes the form of a simple voltage controlled exponential expression while the 'window function' $f(R, v)$ is described by a similar RS and voltage dependent exponential,

which is different from the previously proposed empirical formulations that are expressed as solely state dependent. Notably, the proposed window function allows for the derivation of a predictive analytical RS time-response expression under constant bias voltage $R(t)|_{V_b}$ which greatly simplifies the fitting of the model on characterization data and can be exploited to implement a computationally efficient simulation model that does not require the integration of the state variable equation (dR/dt). Accordingly, the proposed model is suitably coded in Verilog-A which is a behavioral language standardized in the semiconductor industry mainly due to its ease of use and flexibility to run in numerous industrial circuitry simulators (Spectre, HSPICE, Eldo etc.).

The paper is structured as follows: Section II briefly describes the operation theory of the devices fitted by the proposed model. Model functionality and equations are presented in Section III. Section IV analyzes a) the characterization procedure employed on in-house fabricated $TiOx$-based devices and b) the parameter extraction method used to calculate the model parameters from the exported data. Section V validates the proposed model and the parameter extraction algorithm on both valence change memory (VCM) filamentary and non-filamentary ReRAM devices and compares its fitting accuracy against a widely adopted generalized and highly non-linear memristor model. Section VI details the coding strategy utilized to implement a computationally efficient Verilog-A module based on the model expressions while Section VII describes the methods used throughout the manuscript. Finally, in Section VIII certain model characteristics are discussed and the paper is concluded.

II. Operation Theory Captured by the Proposed Model

The previously mentioned generalized models have demonstrated excellent performance in capturing memristive device $I-V$ characterization data responding to different kinds of voltage sweeps (piece-wise linear, sinusoidal etc). Nevertheless, these data enclose only a subset of device switching dynamics. Detailed switching characterization data where device RS is swept in its resistive region of operation for different voltage levels, such as the ReRAM RS responses shown in Fig. 1, have not been fitted in any of these works. The illustrated plots resemble the form of typical VCM and non-filamentary RS responses where regardless of the voltage value applied, we notice an initially steep change in RS followed by gradual saturation. This behavior has been reported by many ReRAM technologies [13], [21], [22], [23], [24], [25], etc.

Focusing on VCM devices, these operate via the formation of oxygen-deficient filaments in transition metal oxides with among the most commonly met examples being the $TiOx$-, $FeOx$- and $TaOx$-based devices for which $R(t)|_{V_b}$ plots are shown in Figs. 1(a), (b) and (c) respectively. Briefly, as oxygen ions are considered more mobile than metal elements, bias application causes the local motion of these defects (oxygen ions) which induces a local valence change of the cations triggering resistive switching [26]. Moreover, in [24] the authors presented a physical model for a VCM $Pt/Ta/TaOx/Pt$ device where

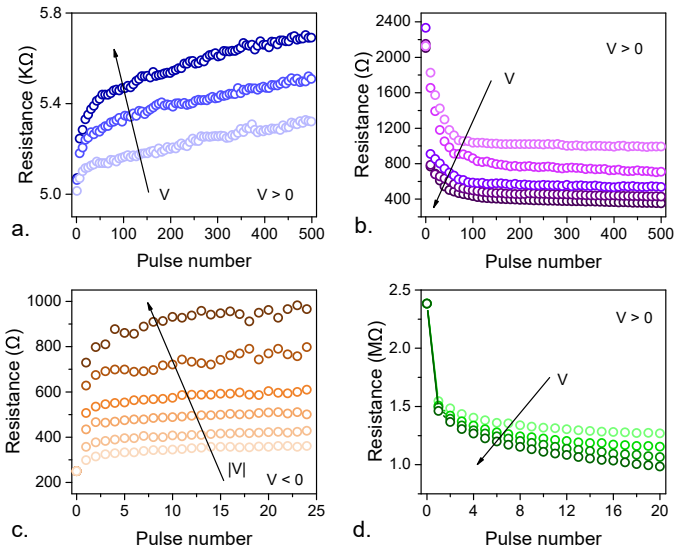

Fig. 1. Typical resistive responses to voltage pulses of constant amplitude reproduced by four different ReRAM technologies: (a) OFF-switching transitions of an in-house fabricated filamentary VCM $TiOx$-based sample. (b) ON-switching transitions for the filamentary VCM $FeOx$-based device presented in [23]. (c) OFF transitions for the filamentary VCM $TaOx$-based device modeled in [24]. (d) ON transitions for the non-filamentary $Ta/TaOx/TiO_2/Ti$ stack modeled in [21]. Sub-plots (b)-(d) were digitized from the corresponding figures in the respective papers.

resistive switching is linked to the radius modulation of a Ta-rich conducting cylindrical-assumed filament surrounded by a matrix of insulating forms of $TaOx$. They consider that two specific competing components of ionic flux, Fick and Soret diffusion, determine a steady state filament radius and resistive state for the device. Specifically, this is defined from the balance between these two diffusion mechanisms which is controlled by the applied voltage, i.e. a specific voltage level ultimately settles the device at a specific RS (see Fig. 1(c)). Regarding the switching mechanism in non-filamentary devices, the authors in [21] presented a $Ta/TaOx/TiO_2/Ti$ stack where resistance change is determined by homogeneous barrier modulation (HBM) induced by oxygen ion migration [27]. Under pulsed voltage stimulation and starting from an initial high RS, the first pulses provoke oxygen ions to drift rapidly from the $TaOx$ bulk toward the $Ta/TaOx$ interface thus lowering device resistance. The accumulated charge (in the anode) reduces the internal electric field which in turn dampens further ion migration toward the interface (saturation). ON-switching responses of the described physical mechanism are illustrated in Fig. 1(d). A similar phenomenon occurs when OFF-switching pulses are applied. Behaviorally, in both VCM and non-filamentary cases, we notice that RS saturation seems to take place at well separated voltage dependent resistive levels.

Conversely to the previously proposed generalized memristor models, the presented model embodies a voltage dependent window function expression which implements voltage dependent rather than constant resistive boundaries of operation, $R_{min}(v)$ and $R_{max}(v)$. As this approach is in tune with commonly met ReRAM behavior (Fig. 1), we will show that the proposed model is able to capture accurately such responses.

III. ReRAM Model

In the proposed ReRAM model both the current-voltage ($I-V$) characteristics and the time derivative of the state variable (dR/dt) are linked to bias voltage v and RS R with the following differential algebraic equation (DAE) set:

$$i(R,v) = \begin{cases} a_p(1/R)\sinh(b_p v), \ for\ v > 0 \\ a_n(1/R)\sinh(b_n v), \ for\ v \leq 0 \end{cases} \tag{3}$$

$$\frac{dR}{dt} = g(R,v) = s(v) \times f(R,v) \tag{4}$$

where $s(v)$ is the switching sensitivity function,

$$s(v) = \begin{cases} A_p(-1+e^{t_p|v|}), \ v > 0 \\ A_n(-1+e^{t_n|v|}), \ v < 0 \\ else\ 0 \end{cases} \tag{5}$$

and $f(R,v)$ corresponds to the window function,

$$f(R,v) = \begin{cases} -1+e^{\eta k_p(r_p(v)-R)}, R < \eta \cdot r_p(v), \ v > 0 \\ -1+e^{\eta k_n(R-r_n(v))}, R > \eta \cdot r_n(v), \ v < 0 \\ else\ 0 \end{cases} \tag{6}$$

Symbols $a_{p,n}$, $b_{p,n}$, $A_{p,n}$, $t_{p,n}$, $k_{p,n}$ are fitting parameters, while $r_{p,n}(v)$ are the voltage dependent resistive boundary functions for the positive and negative stimulation cases which will be discussed in the next paragraph. Parameter η is 1 or -1 depending on the switching direction of device RS to said stimulus polarity. Specifically, for bipolar device functionality, $\eta = 1$ when $\Delta R(V_b) > 0$ for $V_b > 0$ while $\eta = -1$ when $\Delta R(V_b) > 0$ for $V_b < 0$. A sample switching rate surface reproduced by the proposed model (4)-(6) is shown in Fig. 2 which describes changes in the device's state variable because of stimulation given a well-defined initial state R_0 and with a fixed voltage v.

Functions $r_{p,n}(v)$ in (6) take the form of voltage controlled polynomials,

$$r_{p,n}(v) = \sum_{m_{p,n}=0}^{q_{p,n}} r_{m_{p,n}} v^{m_{p,n}} \tag{7}$$

where $m_{p,n}$ are positive integers and $q_{p,n}$ define the order of the polynomials for the positive and negative stimulation cases. Notably, for $m = 0$, resistive boundaries become constant matching the conventional modeling approach. Assuming that $\eta = 1$, (6) calculates zero switching above a specified voltage dependent resistive threshold value $r_p(V_b)$ for $V_b > 0$ and below $r_n(V_b)$ for $V_b < 0$. In agreement with the generic ReRAM behavior shown in Fig. 1, the positions of these resistive limits are monotonically dependent on voltage. The model predicts that higher positive voltages push $r_p(V_b)$ to higher RSs while more invasive negative biases push $r_n(V_b)$ to lower RSs. The physical interpretation of these boundaries is described as follows: for any RS below $r_p(V_b)$ (active region) at a given positive voltage V_b, applying this voltage can push the device to $r_p(V_b)$, but no further (saturation). If the device is already above $r_p(V_b)$, no switching occurs (for positive stimulation). The same applies for negative biasing and the $r_n(V_b)$ limit. Experimentally, the specific functional form of (7) is revealed by utilizing the parameter extraction algorithm described in the Section that follows. For the tested devices: $q_{p,n} \leq 2$ (see Section V).

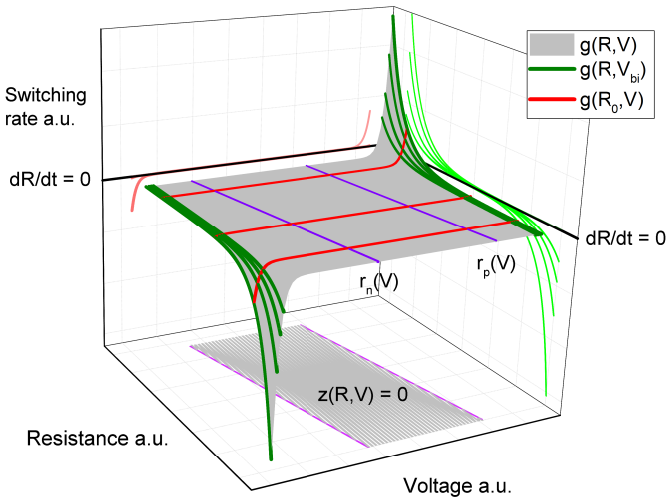

Fig. 2. Example switching rate surface ($g(R,v)$- gray surface) characteristics as reproduced by the proposed switching rate expression (4). Green lines correspond to dR/dt vs R plots for constant bias stimulation V_b ($g(R,\pm V_{bi})$). The characterization routine (see Section IV) is designed to sample the device's switching surface along these lines. Conversely, red lines sample the device's switching surface on lines parallel to the voltage axis ($g(R_0,v)$), though a much more complex testing algorithm is required in order to gather such measurements. Purple lines delineate the voltage dependent resistive boundary functions (7) (in linear form) for the positive $r_p(v)$ and negative $r_n(v)$ stimulation cases. These are projected on the figure base to mark the interface between non-zero (white) and zero (gray) switching regions ($z(R,v) = 0$).

By examining the switching model equations, we notice that the proposed sensitivity function (5) lacks voltage thresholds. Threshold voltage parameters have been adopted by the models presented in [10], [11], [28] as an approximation that neglects the device's low voltage (modeled as sub-threshold) kinetics. Mathematically, these models bear relatively simple switching expressions that are focused in capturing physical device behavior in the over-threshold region, thereby enhancing their ftting performance on $I-V$ characterization data. This approximation is further justified as certain demonstrated practical applications are based on the assumption of ReRAM thresholded behavior [29]. However, the response of a physical device to input voltage doesn't depend solely on voltage but also on current RS which implies that the same device may exhibit different voltage thresholds depending on its running RS ($V_{th}(R)$). This is also captured by our model. Solving (7) with respect to voltage gives us the switching threshold voltage dependency on device RS,

$$V_{th,p,n}(R) = r_{p,n}^{-1}(R) \tag{8}$$

We should note here that for $q > 1$, equation (8) has more than a single solution. The value for $V_{th,p,n}$ corresponds to the solution that is included in the device's operating voltage region. Purple lines in Fig. 2 are reproduced by the resistive boundary function (7) (in linear form for both polarities) which

delineates the zero-switching area $z(R, v) = 0$ (projected at the base of Fig. 2).

Summarizing, a) the presence of RS dependent switching voltage thresholds ($V_{th}(R)$) and b) the variable (rather than constant) voltage dependent window function boundaries are modeled by (6) via the voltage dependency expressed by the resistive boundary function (7), an approach that was initially introduced in the method presented in [30].

IV. Model Fitting to Characterization Data

In order to fit the model on an arbitrary ReRAM device, a proper device-characterization procedure complemented by a parameter extraction algorithm for the proposed model is employed. In this section, we describe the characterization applied on in-house fabricated $TiOx$-based samples similar to the ones investigated in [31], along with the fitting procedure that calculated the model parameters (see Methods for device fabrication details).

Parameters $a_{p,n}$, $b_{p,n}$ were obtained by fitting (3) on multiple static current-voltage responses taken at different RSs during the flow of the characterization protocol.

The parameters for $s(v)$ and $f(R, v)$ were determined by exploiting the simple form of the proposed switching rate expression (4)-(7) which can be solved analytically under constant bias voltage stimulation. Thus

$$R(t)|_{V_b} = \\ = \frac{\ln(e^{\eta k_p r_p(V_b)} + e^{-\eta k_p s_p(V_b) t}(e^{\eta k_p R_0} - e^{\eta k_p r_p(V_b)})}{k_p} \quad (9)$$

$for\ V_b > 0\ and\ R < \eta \cdot r_p(V_b),$

$$R(t)|_{V_b} = \\ \frac{\ln(e^{-\eta k_n R_0 + \eta k_n s_n(V_b) t} - e^{-\eta k_n r_n(V_b)}(-1 + e^{\eta k_n s_n(V_b) t}))}{k_n} \quad (10)$$

$for\ V_b < 0\ and\ R > \eta \cdot r_n(V_b),$

$else\ R_0.$

Parameter R_0 is the initial RS, t is time, $s(V_b)$, $r(V_b)$ are constant valued when the input voltage is fixed, $v = V_b$, and $\eta = \pm 1$ defines the switching direction as discussed in the previous Section. The parameters for the switching member of the proposed model were calculated by repeatedly applying constant voltage stimulation on the device under test (DUT) (at different V_b levels) and fitting (9), (10) to the resulting transient responses. Practically, the device's dynamical behavior is interrogated by sampling its switching rate surface ($g(R, v)$, assumed to be stationary for sufficiently low voltage stimulation) at multiple constant voltage levels V_{bi}, such as the example $g(R, V_{bi})$ plots shown as green lines in Fig. 2.

A. Characterization routine

The characterization routine applied can be described as a two-stage process repeated multiple times in order to gather sufficient information regarding the current-voltage and the switching characteristics of the DUT. An example of this two-stage process is shown in Fig. 3 while a more detailed description of the specific characterization protocol applied on the tested $TiOx$ devices is given in the Methods section. During the first stage, device RS R_0 is read and a triangular, pulsed, sub-threshold voltage sweep is employed (red pulses), such so as to not induce any apparent hysteresis in the resulting $I - V$ response. The outcome is the static $I - V$ characteristic plot at R_0 (Fig. 3(b)). At the second stage, a train of pulses of fixed voltage amplitude and time duration is employed (blue pulses) resulting in the typical resistive response shown in Fig. 3(c) which corresponds to an OFF-switching event. Depending on the polarity of the voltage pulses applied the extracted RS response may match an ON-switching transition instead. At the end of stage 2 the device has switched to a new value R_0', i.e. at the next iteration both steps are repeated having the device initialized from a new initial RS and so on. Throughout this process a) static current-voltage measurements are collected for different RSs (see Fig. 4) and b) switching characterization data is gathered for different voltage levels (of both polarities) starting from different initial RSs (see Fig. 5).

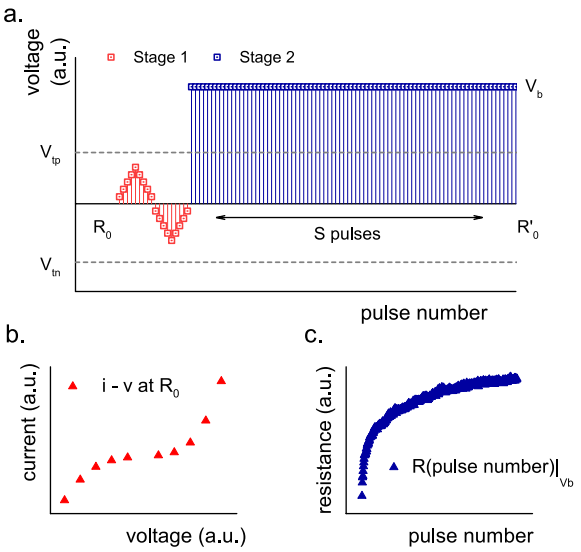

Fig. 3. Example 2-stage characterization sequence and the data exported at every stage of the device testing procedure. (a) Red pulses signify the triangular voltage sweep for capturing the static $I - V$ characteristics at R_0 shown in (b). The second stage applies a train of S identical pulses (blue pulses) and the device RS is read after each pulse is applied therefore capturing the device's RS time-response $R(t)$ during the process, seen in (c).

B. Switching parameter extraction algorithm

We seek for a set of parameter values that collectively fits all exhibited RS time domain responses (Fig. 3(c)) for every voltage level employed (in the observed device dependent voltage space of operation) and for every initial RS sampled. This may be achieved through the following steps.

For the positive stimulation case $v > 0$ the model consists of parameters A_p, t_p, that define the sensitivity function (5) and k_p along with the coefficients for the voltage controlled polynomial $r_p(v)$ (7) that are contained in the window function (6). We

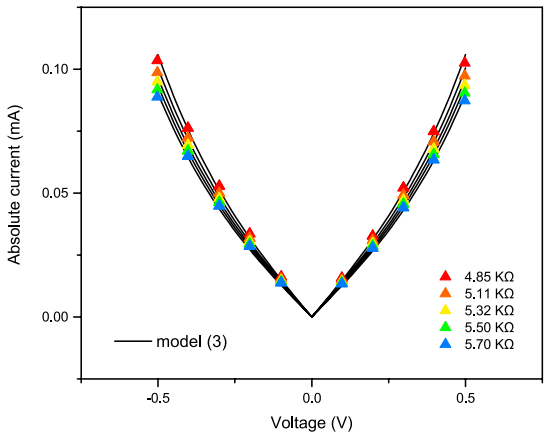

Fig. 4. Static $I-V$ characteristics for DUT 1. A number of 8 sets of $I-Vs$ were exported for different device RSs ranging from $4.85\,\mathrm{K\Omega}$ to $5.70\,\mathrm{K\Omega}$. Only 5 sets are shown for the sake of clarity. The experimental responses shown (colored symbols) were fitted with (3) (solid lines). Parameter values and fitting error are listed in Table I.

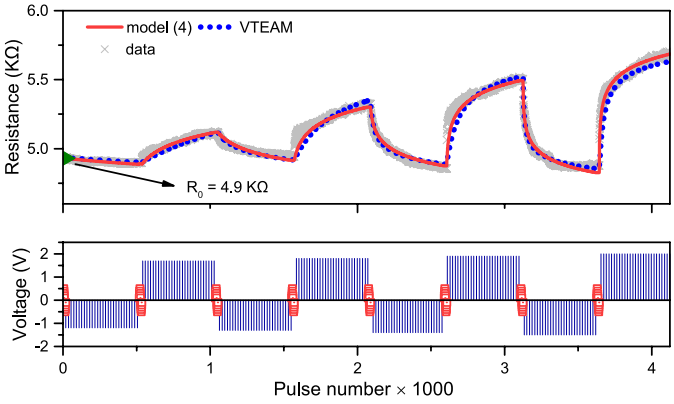

Fig. 5. $Pt/TiOx/Pt$ DUT 1 case study. Bottom trace: Blue vertical lines correspond to pulse trains employed for the purpose of device RS modulation. Red square symbols depict the sub-threshold, triangular, pulsed voltage sweep for static $I-V$ characterization. Top trace: Evolution of measured physical device RS (gray crosses) starting from the initial value R_0 (green symbol) responding to device characterization. Solid and dotted lines are reproduced by the proposed switching model (4) and the VTEAM [10] model respectively. Parameter values for (4) are listed in Table II. VTEAM parameter values are tabulated in the Appendix. % RMS fitting errors are compared in Table III. Characterization routine parameters (see Methods): $t_{w,iv}=1.1\,\mathrm{ms}$, $t_{w,\Delta R}=100\,\mu\mathrm{s}$, $V_{start,n}=-1.2\,\mathrm{V}$, $V_{stop,n}=-1.5\,\mathrm{V}$, $V_{start,p}=1.7\,\mathrm{V}$ and $V_{step}=|0.1|\,\mathrm{V}$.

assume $\eta=1$ (positive biasing causes the device to switch towards higher RSs) and that we have extracted experimental results from multiple voltage levels $V_i, i=1,2,3,....$ The procedure is initiated by fitting an RS response $R(t)|_{V_x}$ that exhibits a clear trend and shape, i.e. it is provoked by a relatively invasive voltage amplitude V_x. Expression (9) is used for this first fitting action and $s_p(V_x)$ is substituted with (5). This fitting determines the parameter values A_p, t_p along with k_p and $r_p(V_x)$ at the same voltage level.

Next, the defined A_p, t_p, k_p parameter values are used to perform the same fitting on data for the remaining voltage levels which determine points on $r_p(V_i)$. Fitting these to the corresponding voltage controlled polynomial $r_p(v)$ (7) determines its coefficients.

The same procedure applies on the negative stimulation case ($v<0$) where equation (10) is used instead.

V. Fitting Results

In this section, we validate the fitting performance of the presented model and the proposed parameter extraction algorithm. The overall root mean square (RMS) error is defined as $3.19\,\%$ for the presented static $I-V$ fits and $2.07\,\%$ for the fitted dynamic resistive responses. Specifically we fitted: a) 2 in house fabricated $Pt/TiOx/Pt$ VCM devices, b) the $Pt/Ta/TaOx/Pt$ VCM device modeled in [24] and c) the non-filamentary $Ta/TaOx/TiO_2/Ti$ device modeled in [21]. The illustrated static $I-Vs$ were fitted with (3) bearing the parameter values listed in Table I. Dynamic resistive switching responses were fitted with (4)-(7) with the parameter values listed in Table II.

A. $Pt/TiOx/Pt$ case

1) DUT 1: The experimental static $I-V$ characteristics of Fig. 4 (colored symbols) are typical responses exhibited by the $TiOx$ samples fitted in this work where the maximum absolute voltage applied in the triangular pulsed excitation (see Methods) was kept below $|0.5|\,\mathrm{V}$ to prevent the device from switching. The $I-V$ model performance (3) is illustrated with black solid lines. % RMS fitting errors are listed in Table I.

TABLE I
Parameter values and RMS errors for static $I-V$ fits with (3)

Device	a_p	a_n	b_p	b_n	% RMS error
$TiOx$	0.24	0.24	2.81	2.81	2.49
[24]	0.36	0.34	1.83	3.50	3.89

We should comment here that at a first glance, equation (3) reads very similar to the $sinh$-based current-voltage relationships adopted by the models in [11] and [12],

$$i = Axsinh(Bv) \tag{11}$$

where A, B are fitting parameters and x is the state variable. Nevertheless, their port equations are proportional to their internal state variable x which is limited in the interval $[0,1]$. According to their state variable mechanism, for $R=R_{max} \Leftrightarrow x=0 \Leftrightarrow i=0$ which is fundamentally unrealistic behavior that limits their applicability.

Fig. 5 (top trace) demonstrates the dynamical behavior of physical (gray crosses) versus simulated device RS (red line) under the characterization routine (bottom trace). Multiple ON- and OFF-switching responses for various voltage levels starting from different initial RSs are fitted with excellent accuracy. The RS boundary functions, $r_p(v)$, $r_n(v)$ (7), are used in linear form for both biasing polarities (see Table II).

2) DUT 2: For DUT 2 we focus solely on its switching behavior. Fig. 6 (top trace) compares experimental (pale gray crosses) with fitted (red line) RS responses under the characterization routine for model parameter extraction (bottom trace) demonstrating once more excellent performance. A constant resistive boundary value $r_p \equiv R_{max}$ is used for $v>0$

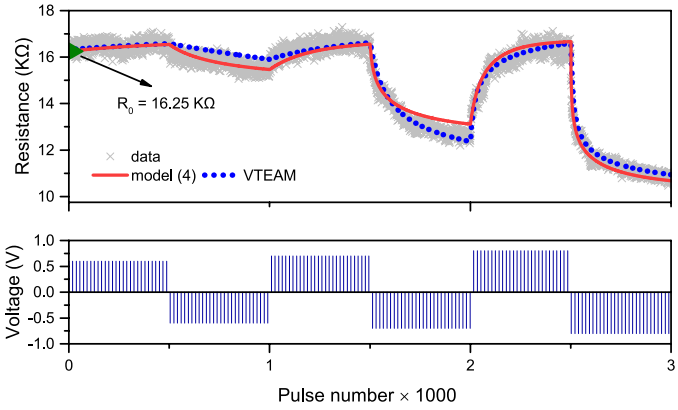

Fig. 6. $Pt/TiOx/Pt$ DUT 2 case study. Bottom trace: Blue vertical lines depict the pulse trains employed to modulate device RS. Only the switching mode of the characterization routine is utilized for this device. Top trace: Gray crosses belong to physical device measurements. Solid and dotted lines are reproduced by the proposed switching model (4) and the VTEAM model [10] respectively. Parameter values for (4) are listed in Table II. VTEAM parameter values are tabulated in the Appendix. % RMS fitting errors are compared in Table III. Characterization routine parameters (see Methods): $V_{start,p} = 0.6\,\mathrm{V}$, $V_{stop,p} = 0.8\,\mathrm{V}$, $V_{start,n} = -0.6\,\mathrm{V}$ and $V_{step} = |0.1|\,\mathrm{V}$.

TABLE II
PARAMETER VALUES THAT FIT THE PROPOSED SWITCHING MODEL (4) ON THE CASE STUDY DEVICES

Para-meters	$TiOx$ (DUT 1)	$TiOx$ (DUT 2)	$TaOx/TiO_2$ [21]	$TaOx$ [24]
A_p	0.12	743.47	$-2.06 \cdot 10^5$	$-6.82 \cdot 10^6$
A_n	−79.03	$-6.80 \cdot 10^4$	3.66	$7.25 \cdot 10^7$
t_p	0.59	6.51	0.38	1.08
t_n	1.12	0.31	0.015	0.036
k_p	$8.10 \cdot 10^{-3}$	$5.11 \cdot 10^{-4}$	$6.13 \cdot 10^{-6}$	0.017
k_n	$9.43 \cdot 10^{-3}$	$1.17 \cdot 10^{-3}$	$2.17 \cdot 10^{-6}$	0.018
r_{p0}	3085	$16.71 \cdot 10^3$	$1.23 \cdot 10^7$	2794
r_{p1}	1862	0	$-2.39 \cdot 10^6$	−4553
r_{p2}	0	0	$1.21 \cdot 10^5$	1973
r_{n0}	5193	$29.30 \cdot 10^3$	$1.29 \cdot 10^7$	857
r_{n1}	378	$23.69 \cdot 10^4$	$58.07 \cdot 10^4$	1135
r_{n2}	0	0	$56.45 \cdot 10^3$	675

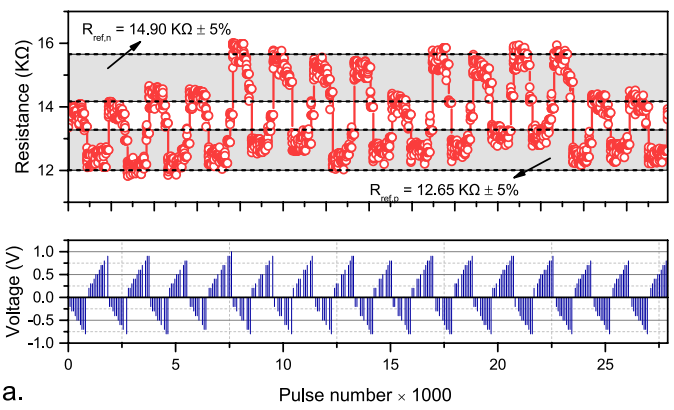

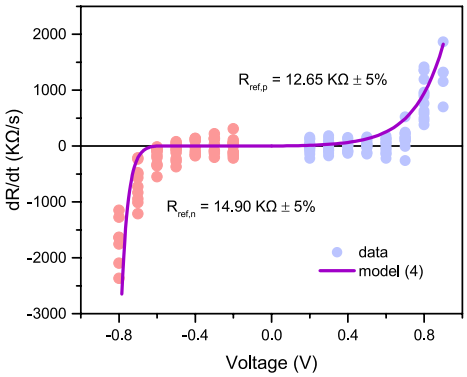

Fig. 7. $Pt/TiOx/Pt$ DUT 2 case study. Model validation on alternative device testing. (a) Bottom trace: Application of successive incremental step pulse train ramps (ISPTR) for the purpose of gathering switching data of the form $\Delta R(R_0, v)$. The demonstrated ISPTR-based testing algorithm is thoroughly analyzed in [7]. ISPTR testing routine parameters: $N = 10\,\mathrm{pulses/train}$, $t_w = 100\,\mu\mathrm{s}$. Top trace: Resistive response of DUT 2 to alternative device testing. Gray shadings highlight the most data-populated resistive bands for ON and OFF transitions with a tolerance of $\epsilon_{ref} = 5\,\%$ around their central resistive values ($R_{ref,p}$, $R_{ref,n}$). (b) Pale blue symbols approximate $dR(R_{ref,p}, v)$ switching data exported by the ISPTRs applied. Pale red symbols approximate $dR(R_{ref,n}, v)$ switching data. Purple solid line is reproduced by the proposed switching model (4) bearing the parameters exported by the proposed parameter extraction algorithm and the testing shown in Fig. 6.

while for $v < 0$, function $r_n(v)$ is utilized in linear form (see Table II).

One further test regarding the switching behavior of DUT 2 was performed and is shown in Fig. 7(a) (bottom trace). Conversely to the characterization routine for model parameter extraction (Fig. 6) which was focused on gathering switching data under constant bias voltage application ($\Delta R(R, V_b)$), we employed a testing algorithm previously presented in [7], so as to characterize the device's switching characteristics around the same initial RS R_0 for multiple voltage levels ($\Delta R(R_0, v)$). The algorithm operates by employing pulsed voltage ramps of alternating polarities and the bipolar DUT behavior exhibiting OFF transitions under positive voltage bias and ON transitions under negative, was exploited in order to restrict DUT RS within a narrow resistive range (Fig. 7 - top trace). Each ramp level was a pulse train that consisted of N pulses/train with fixed duration t_w (see figure caption). As device RS was read and stored after each pulse train applied, the RS around which most gathered data was clustered was defined as the central value of R_x for which the interval $[R_x - \epsilon_{ref}, R_x + \epsilon_{ref}]$ contained the maximum number of data points. We then considered that these data points could be used to determine $\Delta R(R_x, v)$ as a fair approximation.

Fig. 7(b) plots switching rate data (round colored symbols) as a function of bias voltage for $\epsilon_{ref} = 5\,\%$. For OFF transitions, the most populated interval had its center at $12.65\,\mathrm{K\Omega}$ while for ON transitions this was defined at $14.90\,\mathrm{K\Omega}$. The purple line in Fig. 7(b) was reproduced by the proposed switching rate model (4) with the parameter values extracted from the initial device testing (Fig. 6) showing good agreement with the measured results thereby supporting the initial assumption of switching rate surface stationarity (Fig. 2).

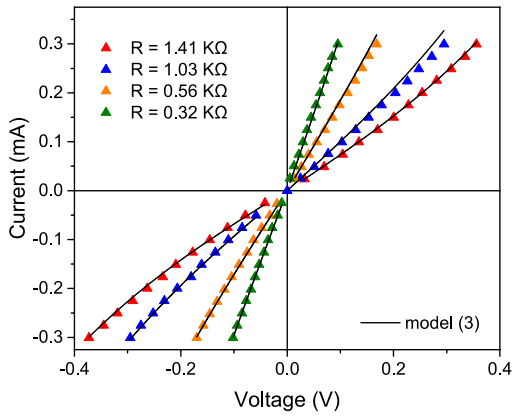

Fig. 8. Fitted static current-voltage characteristics of the $Pt/Ta/TaOx/Pt$ device presented in [24] with (3). Symbols correspond to data points digitized from Fig. 4 of the same work. Device RS was defined at the positive read voltage of $V_{read} = 0.1\,\mathrm{V}$. Parameter values and fitting error for (3) are listed in Table I.

TABLE III
% RMS FITTING ERRORS OF THE TESTED DYNAMIC MODELS ON DIFFERENT DEVICE CHARACTERIZATION DATA

Device	Model (4)	VTEAM (12)	DUT RS range
$TiOx$ - DUT 1	0.52 %	0.88 %	$4.5\,\mathrm{K\Omega} - 6.0\,\mathrm{K\Omega}$
$TiOx$ - DUT 2	2.18 %	2.19 %	$10\,\mathrm{K\Omega} - 17\,\mathrm{K\Omega}$
$TaOx$ - [24]	3.27 %	15.54 %	$200\,\Omega - 1000\,\Omega$
$TaOx/TiO_2$ - [21]	2.32 %	4.49 %	$1\,\mathrm{M\Omega} - 4\,\mathrm{M\Omega}$

B. $Pt/Ta/TaOx/Pt$ case

Fig. 8 demonstrates the static $I - V$ fits of the device presented in [24] with the proposed model (3). The % RMS fitting error is listed in Table I.

In Fig. 9 resistive responses are plotted (pale green symbols) as a function of applied voltage pulse number for multiple ON- and OFF- switching transitions provoked by different constant voltage levels. Green lines match the fitting performance of the proposed switching model (4). For this case, the $r(V_b)$ points extracted by the testing routine were fitted with a 2nd order expression (see Table II).

C. $Ta/TaOx/TiO_2/Ti$ case

Fig. 10 compares measured (pale blue symbols) versus simulated (blue lines) RS responses to pulse stimulation for the analog ReRAM device presented in [21]. Model and experimental results are once again in very good agreement. As with the previous device case study, (7) takes the form of a 2nd order expression (see Table II).

The % RMS errors regarding the accuracy of the switching model (4) on the RS responses of Figs 5, 6, 9, 10, are concentrated in Table III. Fitting errors indicate that the proposed model can be used to fit a wide range of devices with sufficient accuracy by employing the compact parameter extraction method presented in Section IV.

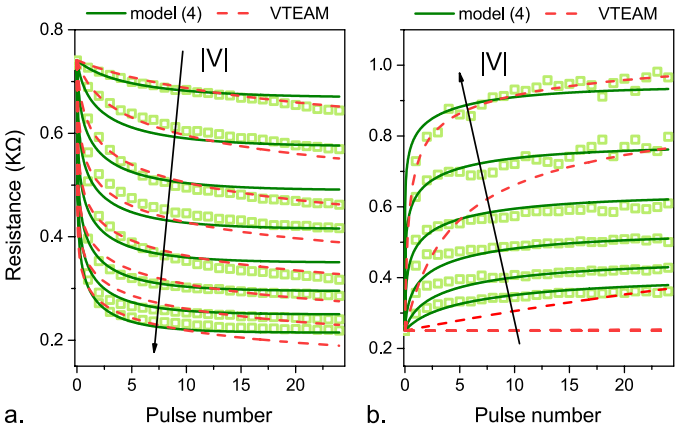

Fig. 9. $TaOx$-based device case study ([24]). Figure illustrates RS responses versus voltage pulse number for different voltage levels for (a) ON- and (b) OFF-switching transitions. Symbols correspond to RS data measured at $V_{read} = 0.05\,\mathrm{mV}$. Data points were digitized from Fig. 3 in [24]. Solid green line matches the proposed switching model (4) while red dashed line matches the VTEAM model [10]. (a) For $v > 0$: $V_b = 0.65\,\mathrm{V} \rightarrow 1\,\mathrm{V}$, $V_{step} = 0.05\,\mathrm{V}$. (b) For $v < 0$: $V_b = -1\,\mathrm{V} \rightarrow -1.75\,\mathrm{V}$, $V_{step} = -0.15\,\mathrm{V}$. Parameter values for (4) are listed in Table II. VTEAM parameter values are tabulated in the Appendix. % RMS fitting errors are compared in Table III.

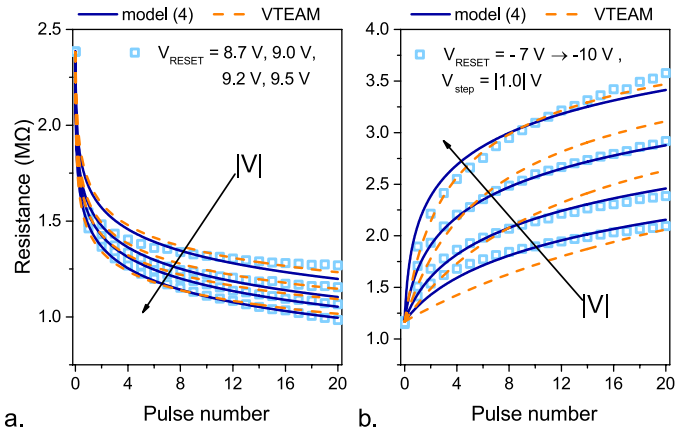

Fig. 10. $Ta/TaOx/TiO_2/Ti$ device case study ([21]). Symbols correspond to experimental a) ON and b) OFF RS transitions measured at $V_{read} = -2\,\mathrm{V}$. Data points were digitized from Fig. 6 in the relevant manuscript. In both panels solid lines match the proposed model (4) while dashed lines are reproduced by the VTEAM model [10]. Parameter values for (4) are listed in Table II. VTEAM parameter values are tabulated in the Appendix. % RMS fitting errors are compared in Table III.

D. *Comparison with a previously proposed generalized, highly non-linear memristor model*

Among the generalized, well established memristor models published till know, we compare the accuracy of the proposed model in capturing the dynamical RS responses shown in the previous subsections versus the VTEAM model presented in [10]. The state variable equation in the VTEAM model consists of a threshold-equipped sensitivity function $s(v)$, expressed with an α-power law function, which is much more flexible than the simple exponential proposed by Yakopcic [11] or the $sinh$ forms proposed by Laiho [12] and Chang [13]. For the VTEAM model, any window function implementation can be coupled with the sensitivity function $s(v)$ ([16], [17], [32]). In our case study, we utilize a modified version of the

approximation of the Simmons tunnel barrier model presented in [17], which is particularly non-linear and is expressed with a double exponential function for both biasing polarities. The benchmarked switching model reads,

$$\frac{dx}{dt} = \begin{cases} k_{off}(\frac{v}{u_{off}} - 1)^{a_{off}} e^{-e^{x/x_{off}}}, v > u_{off} > 0 \\ k_{on}(\frac{v}{u_{on}} - 1)^{a_{on}} e^{-e^{-(x-1)/x_{on}}}, v < u_{on} < 0 \\ else\ 0 \end{cases} \tag{12}$$

where k_{off}, k_{on}, a_{off}, a_{on} ,x_{off}, x_{on} are fitting parameters and u_{off}, u_{on} are the threshold voltages. In (12), the state variable x is dimensionless and practicaly bound in the interval $[0, 1]$ while increasing its value increases device resistance.

Figs. 5, 6, 9, 10 demonstrate the fitting performance of (12) on the corresponding physical device characterization data. For the $Pt/TiOx/Pt$ devices signified as DUT 1 and DUT 2, both models present similar accuracy while for the filamentary $TaOx$-based and non-filamentary $Ta/TaOx/TiO_2/Ti$ devices our model outperforms the implementation expressed with (12). % RMS errors are compared in Table III.

As with every other generalized memristor model, in order to fit the VTEAM model on the ReRAM case study responses shown, the application of certain iterative processes such as simulated annealing algorithms and gradient descend are required. Here, we invoked the Eureqa Nutonian A.I. (Artificial Intelligence) powered modeling engine software [33]. Eureqa supports the modeling of derivatives, thus RS time-responses for each tested device and polarity were fed to this fitting software which exported the best parameter values for the state derivative expression (12). The data processing for linking device RS measurements (R) with state variable values (x) along with the parameter values for (12) can be found in the Appendix.

On the other hand, the model presented in Section III via its analytical time response expressions (9), (10) determines the most suitable parameter values for an $R(t)|_{Vb}$ response in a single step, allowing the design of the parameter extraction method described in Section IV. The method is powerful as it can easily adapt on noisy and/or sparsely populated data sets, general as it can fit different types of ReRAM devices and technologies but also extremely practical. This was demonstrated in [34], where a slightly modified version of this algorithm was integrated in a characterization platform previously described in [20]. There, we used the system-available Python interface to a) program the appropriate experimental routine, b) apply the testing on the device and c) analyze the exported data to fit ReRAM devices on the corresponding model expressions. Impressively, all operations were carried out extremely fast (approximately 3 minutes per fitted sample) at a click of a button.

VI. Verilog-A Model

In every memristor computer model published so far [10], [11], [15], [35], [36], [37] the memory effect of the memristor is modeled by solving numerically the corresponding model DAE set. SPICE models perform numerical integration with the use of a feedback controlled integrator circuit where the value of

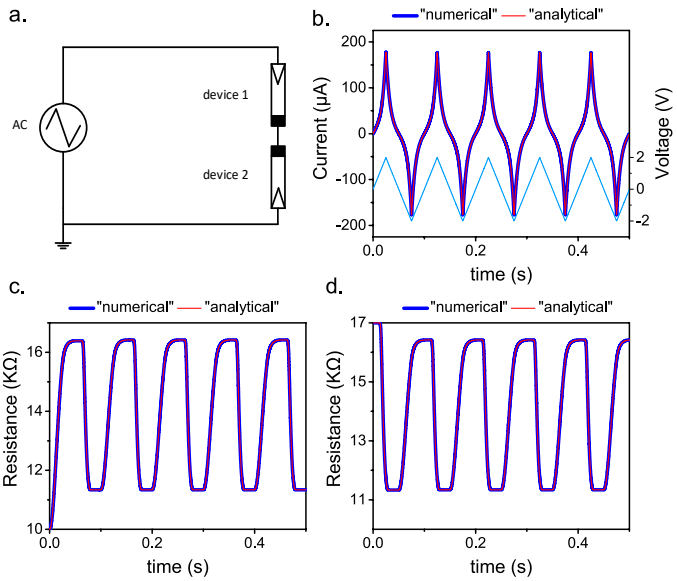

Fig. 11. Comparison of the 'numerical' (blue line) against the 'analytical' (red line) model implementations on the test circuit drawn in (a). Panel (b) plots the triangular input voltage excitation applied on the anti-series connection of the devices shown in (a) and compares the circuit's current responses. Panels (c) and (d) plot the RS responses of device 1 and device 2 during the simulation. Both devices were simulated with parameters that corresponded to the $Pt/TiO_2/Pt$ device referred as DUT 2 in Section IV.

the devices state variable is represented by the voltage across a unitary capacitance which serves as an integrator of the internal state variable function. The Verilog-A (VA) models presented in [38], [39] perform state variable integration by implementing in-code the forward Euler method as a finite difference method for numerical approximation of integration. Nevertheless, these VA implementations do not make use of the simulator's dedicated integration algorithms which are particularly useful in large scale simulations where the well-established ReRAM models have been reported to present convergence issues [11], [40].

In the suggested VA model the time-evolution of RS (the state variable for the proposed model) is calculated analytically thus in a less compacted fashion (the integration process is omitted) and therefore faster. Our approach exploits that throughout the simulation and for the duration of each time-step used by the simulator, the voltage across the proposed voltage-controlled ReRAM model is fixed, i.e. the resistive state time-response is solved analytically with equations (9), (10). The use of these requires that the initial RS at the beginning of every time-step and the duration of each time-step are tracked during the simulation which can be carried out with proper VA coding. The module that follows the described modeling strategy will be refered from here after as the 'analytical' model.

Here, we validate the proposed 'analytical' implementation in the test circuit shown in Fig. 11(a). This is composed by the anti-series connection of two ReRAMs driven by a triangular voltage source. ReRAM devices match the fitted $Pt/TiO_2/Pt$ case referred as DUT 2 in the preceding section. Results are compared with those exported from simulations that perform numerical integration of the model's DAE set (see 'numerical' model in Methods). The accuracy of the proposed implementation is verified as analytical and numerical

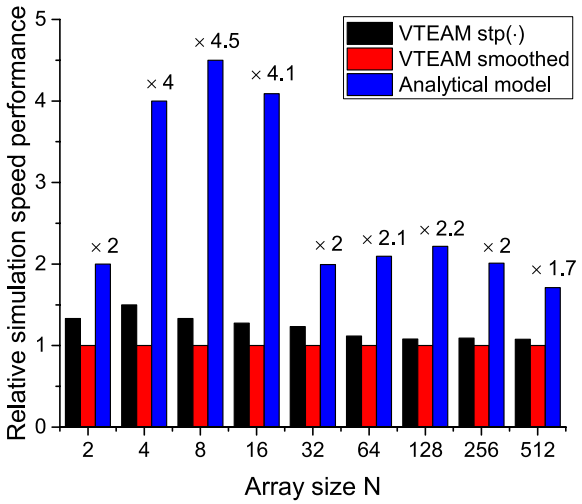

Fig. 12. Relative simulation speed performance versus crossbar size for three Verilog-A implementations that model the behavior of the physical $Pt/TiOx/Pt$ device referred as DUT 1 in Section V. Blue columns correspond to the proposed analytical model while red and black columns match two alternative Verilog-A implementations of the benchmark model. The smoothed VTEAM model (red columns) utilizes (13) in order to smooth all discontinuous piece-wise functions included in the model's equations. Black columns are again reproduced by the VTEAM model where all piece-wise functions are implemented with the use of the discontinuous step function. Simulation time results are normalized according to the smoothed VTEAM model measurements. The proposed 'analytical' implementation is on average $\times 2.73$ faster than the smoothed VTEAM model.

responses are practically matched. In Fig. 11, the triangular input excitation and test circuit current response are plotted in (b) while the RS responses for the two anti-series connected devices are shown in (c) and (d). The amplitude and period for input stimulus are $V_{amp} = 2\,\mathrm{V}$ and $T = 0.1\,\mathrm{s}$ respectively. For the simulation the maximum time step was chosen 0.1% of the input signal period. The simulation speed-up in both circuits averaged on 10 runs was $\times 1.9$ for the circuit shown in Fig. 11(a). The VA codes ('numerical' and 'analytical') for the proposed ReRAM model can be found in [41].

We conclude this section by comparing the proposed analytical model presented in Section V with the VA implementation of the VTEAM model expressed with (12) for which the 'numerical' VA coding approach was followed (see Methods). Model parameters matched the $Pt/TiOx/Pt$ DUT 1 device presented in Section V. As the $I - V$ relationship is not inherently defined in the VTEAM model, expression (3) was utilized for this case with the parameter values listed in Fig. 3 (DUT 1). The simulation speed-up achieved by our proposed analytical expression was evaluated by simulating with both models an OFF- followed by an ON- switching event applied on an entire row of an $N \times N$ selector-less crossbar for various array sizes. Switching was induced by applying voltage pulses (with suitable values for pulse amplitude and duration) to modulate the RS of the devices. The parasitic line resistances were included only to add complexity to the simulated system, thus, their values were defined unrealistically low, such so as to allow switching in every device consisted in the row and at the same time impose different biasing conditions at the terminals of the devices. Our goal was to benchmark the simulation speed performance for the compared implementations in a large-scale ReRAM circuit. Fig. 12 plots simulation speed vs crossbar size N. The proposed analytical implementation is on average $\times 2.73$ faster than the benchmark model.

VII. Methods

A. Device fabrication and preparation

The in-house $TiOx$-based samples tested (DUT 1, DUT 2) correspond to micrometer-scale devices featuring a metal-insulator-metal structure. The process flow started by thermally oxidizing a 6-inch Silicon wafer to create a layer that serves as an insulator medium. Then, three major steps were realized to obtain the bottom electrode, active layer and top electrode consecutively. Each step consisted of optical lithography, material deposition and lift-off process. The $10\,\mathrm{nm}$ platinum layers were deposited for top electrode and bottom electrode by electron beam evaporation, whilst $25\,\mathrm{nm}$ TiO_2 was deposited by reactive magnetron sputtering. These fabrication steps resulted in a metal-insulator-metal stack of $Pt(10\,\mathrm{nm})/TiO_2(25\,\mathrm{nm})/Pt(10\,\mathrm{nm})$ devices. Before use, all devices were electro-formed using positive polarity (top electrode at higher potential than bottom electrode) pulsed voltage ramps. A series resistor was used as a current limiting mechanism in all cases. Typical electro-forming voltages were in the range of $7\,\mathrm{V} - 8\,\mathrm{V}$. Fabrication details for the $Ta/TaOx/TiO_2/Ti$ and $Pt/Ta/TaOx/Pt$ devices can be found in [21] and [24] respectively.

B. Characterization routine parameters

The characterization algorithm applied on the $TiOx$-based devices is summarized in Fig. 3 and thoroughly illustrated in Fig. 5. It consisted of multiple pulse trains of S identical pulses of fixed pulse duration $t_{w,\Delta R}$ where each applied train had its own voltage level V_b defined. Pulse trains were interleaved by triangular sub-threshold pulsed voltage sweeps ($\leq |0.5|\,\mathrm{V}$) with fixed pulse duration $t_{w,iv}$ which exploited the RS modulation provoked by the pulse trains and captured static $I-V$ characteristics at multiple RSs of the device under test. In its flow, the algorithm was carried out by changing polarity with each applied train and increasing the amplitude every two trains by a defined voltage step V_{step}. The absolute amplitude of the negative pulses applied scaled according to V_{step} from an initial voltage $V_{start,n}$, up to a user defined value $V_{stop,n}$ determining the voltage interval of characterization $\Delta V_c = |V_{start,n} - V_{stop,n}|$. Similarly, the positive pulse trains applied, starting from $V_{start,p}$ scaled with the same voltage step V_{step} up to $V_{stop,p} = V_{start,p} + \Delta V_c$ and the algorithm was terminated after pulse trains featuring the final characterization values of both polarities ($V_{stop,n}$, $V_{stop,p}$) were applied. The specific parameters of the characterization routine employed on the device under test are given in the caption of Figs. 5 and 6. RS data was gathered throughout the flow of the algorithm as the initial device RS R_0 and the RS after each single pulse applied were measured. Regardless of the modulated voltage value used to bias the device for the purposes of switching, all assessments of RS for the $TiOx$ devices were carried out at the standard voltage $V_{read} = 0.5\,\mathrm{V}$.

C. Data transformation

In order to fit the analytical expression (9), (10) to the responses reproduced by the tested devices, each pulse was multiplied by its duration ($t_{w,\Delta R}$), thus, the $R(pulse\,no.)$ responses shown in Figs. 5, 6, 8, 9 were transformed into $R(t)$ responses. Pulse rise/fall times were neglected as they comprised only a small fraction of the total pulse duration $t_{w,\Delta R}$.

D. Instrumentation

All experiments were carried out using an upgraded version of the in-house instrumentation previously described in [20].

E. 'Numerical' Verilog-A code implementation

The numerical VA module solves the models DAE set (3)-(7) with the use of the built in VA time-domain integration operator $idt(\cdot)$ which utilizes simulator dedicated numerical integration algorithms. As a continuous and differentiable mathematical description is a mandatory requirement for proper operation of the iterative solution methods used by differential solvers, all discontinuous piecewise model functions were reshaped with the use of the continuous sigmoid approximation,

$$\theta_i(x) = 1/(1 + exp(-x/b_i) \tag{13}$$

Parameter b_i controls the slope of the sigmoid function around the discontinuous corner points imposed by piecewise functions. Its value was adjusted accordingly to facilitate simulator convergence and to keep the models dynamics practically unaffected. For the functions that involved voltage controlled conditionals (5), b_i was modified as, $b_v = 10^{-6}$. For RS related conditionals (6), $b_R = 10^{-3}$. Finally, the steepness of the exponential function in (13) may impose numerical overflows during the simulation. This was dealt by using the limiting exponential function $limexp(\cdot)$ which bounds potentially overflowed values by linearizing the exponential response after an internally defined threshold [42].

VIII. Discussion and Conclusion

In this work, we have presented a behavioral ReRAM model that fits static $I-V$ characteristics and the switching behaviors of typical VCM and non-filamentary ReRAM technologies. The presented model is engineering-friendly as it captures changes in the device's internal state variable as projected macroscopically on its RS. The proposed window function expression is simple, allowing the derivation of an analytical RS time-response expression for constant bias voltage application ($R(t)|_{V_b}$) which offers a predictive capability for the model that can be exploited practically in multiple ways. Here, the analytical expressions (9), (10) were utilized to directly fit physical RS time-responses of a) 2 in-house fabricated VCM $TiOx$-based devices, b) a VCM $TaOx$-based device ([21]) and c) a non-filamentary $TiOx/TaO_2$ device ([24]), all of which are tested under the constant biasing conditions imposed by the compact characterization routine presented in Section IV-A. The use of (9) and (10) rendered a powerful and general method that optimized the parameter values by exploiting the clear shape and trend of the device's RS responses to constant voltage application ($R(t)|_{V_b}$) rather than extracting and working on measured amount of switching (ΔR) values which in general are particularly noisy. The fitting performance of this approach is demonstrated in Figs. 5, 6, 9, 10 showing excellent efficiency on measured RS time-responses. The overall average % RMS error for both static $I-V$ and dynamic measurements is 2.63%. The plots shown in these figures are characteristic resistive time-responses of MOx ReRAM devices which are also met in the WOx-based device presented in [13], the $FeOx$-based device in [23], the Ag/Si device in [25], etc. Moroever, as $TiOx$ devices (also fitted in this work) are considered prototypical for all VCM devices ([43]), it is reasonable to assume that the proposed model is able to account for this broader class of ReRAM devices. Whilst the VCM and non-filamentary device cases cover practically all metal-oxide devices, there are other families of memristive, such as STT- (Spin-transfer torque) and FeRAM-based, (Ferroelectric RAM) devices. The model has not been constructed to fit such cases, however the extent to which the fundamental principles used to build the model are transferable to these is a topic for further investigation.

The proposed model form is explicitly designed to capture the $I-V$ characteristics of devices and their data-derived switching behavior. In order to build more general technology-level rather than device-level models the parameter extraction procedure must be applied a) on the same device, b) on many devices repeatedly, in order to capture cycle-to-cycle and device-to-device variation respectively. Performing a large number of tests on the same device will offer useful information regarding the stability of the model, i.e. for how long the extracted parameters are still an accurate description of the tested device. Assuming the device presents variable behavior, each testing applied will lead to a new set of parameters. Thus, performing multiple tests will have the device trace a trajectory in model parameter space that will reveal both intrinsic cycle-to-cycle variability and perhaps longer trends causing the underlying parameters of the model to fundamental drift as the device ages/is used. Similarly, for device-to-device variability, the routine must be ran on multiple devices and then parameters extracted in order to build a statistical model of the technology being studied which will manifest itself as a technology-dependent joint probability distribution. With enough measurements taken, statistically significant results can be extracted in order to differentiate between in-wafer and inter-wafer variation. But in all cases, the model extraction routine presented is the unit cell that is used to generate each and every data point. As the proposed model expressions are under constant extension and upgrade, other non-ideal effects, such as temperature dependence, are being currently incorporated into the modeling procedure.

Finally, (9) and (10) were exploited to implement a fast computer model that does not require the integration of the model's DAE set, which is a substantial benefit when it comes to large scale ReRAM-based simulations. The proposed model was compared with a previously proposed highly non-linear generalized memristor model showing both increased accuracy and simulation speed. All in all, its general nature and validated performance render this model a practical proposal for enabling

TABLE IV
PARAMETER VALUES FOR THE STATE VARIABLE EQUATION (12) IN THE VTEAM MODEL

Parameters	$TiOx$ (DUT 1)	$TiOx$ (DUT 2)	$TaOx/TiO_2$ [21]	$TaOx$ [24]
k_{on}	-400	$-1.20 \cdot 10^5$	$-1.3 \cdot 10^{-2}$	-5.29
k_{off}	3100	2150	12.81	$6.73 \cdot 10^4$
u_{on}	0.50	0.50	2.00	0.25
u_{off}	1.10	0.50	-2.00	-0.60
e_{on}	4.65	6.00	14.75	16.39
e_{off}	8.69	1.00	5.00	4.14
w_{con}	0.45	0.43	0.39	0.39
w_{coff}	0.39	$3.37 \cdot 10^{-4}$	0.44	0.50
R_{min}	$4850\,\Omega$	$10\,\mathrm{K}\Omega$	$0.9\,\mathrm{M}\Omega$	$200\,\Omega$
R_{max}	$6000\,\Omega$	$2\,\mathrm{K}\Omega$	$4.2\,\mathrm{M}\Omega$	$1000\,\Omega$

informed memristor-based system design before committing to silicon implementations.

APPENDIX

In this section we define the link between state variable x and physical device RS measurements R for the Simmons-based expression (12) and describe the procedure followed to the end of extracting the most suitable parameter values for the corresponding dynamic fits shown in Section V via the Eureqa fitting software tool [33].

State variable and resistance (at a specific read voltage V_{read}) are linked with the following equation,

$$x = \frac{R - R_{min}}{R_{max} - R_{min}} \tag{14}$$

where R_{min}, R_{max} are the window function boundaries. We notice that for $R = R_{min} \Leftrightarrow x = 0$ and for $R = R_{max} \Leftrightarrow x = 1$ which agrees with the state variable mechanism of the investigated model. Accordingly, switching rates are linked with,

$$\frac{dx}{dt} = \frac{1}{R_{max} - R_{min}} \frac{dR}{dt} \tag{15}$$

As the experimental data were either noisy (Figs. 5, 6) or sparsely populated (Figs. 9, 10), all physical RS responses were initially fitted with the minimum mean average error (MAE) that could be achieved by a log-based function. The fitted data sets, rather than the initial raw data points, were then fed to the fitting software (Eureqa) that in turn calculated the most suitable parameter values for expression (12) based on the MAE fitting criterion. Specifically, for the $TaOx$-based responses shown in Fig. 9, in order to improve the fitting result for the OFF- transition cases, the data that corresponded to the three most invasive responses ($V_b = -1.75V$, $-1.60V$, $-1.45V$) were given increased weights relative to the rest data sets. Notably, the only response fitted accurately was the most invasive ($V_b = -1.75V$). Fitting results are shown in Section V while the exported parameter values are listed in Table IV.

REFERENCES

[1] D. B. Strukov, G. S. Snider, D. R. Stewart, and R. S. Williams, "The missing memristor found." *Nature*, vol. 453, no. 7191, pp. 80–3, 2008.

[2] L. O. Chua, "MemristorThe Missing Circuit Element," *IEEE Transactions on Circuit Theory*, vol. 18, no. 5, pp. 507–519, 1971.

[3] Bedeschi *et al.*, "A bipolar-selected phase change memory featuring multi-level cell storage," in *IEEE Journal of Solid-State Circuits*, vol. 44, no. 1, 2009, pp. 217–227.

[4] A. F. Vincent *et al.*, "Spin-transfer torque magnetic memory as a stochastic memristive synapse for neuromorphic systems," *IEEE Transactions on Biomedical Circuits and Systems*, vol. 9, no. 2, pp. 166–174, 2015.

[5] T. Prodromakis, K. Michelakis, and C. Toumazou, "Switching mechanisms in microscale memristors," *Electronics Letters*, vol. 46, no. 1, p. 63, 2010.

[6] S. Gaba, P. Sheridan, J. Zhou, S. Choi, and W. Lu, "Stochastic memristive devices for computing and neuromorphic applications." *Nanoscale*, vol. 5, no. 13, pp. 5872–8, 2013.

[7] A. Serb, A. Khiat, and T. Prodromakis, "An RRAM Biasing Parameter Optimizer," *IEEE Transactions on Electron Devices*, vol. 62, no. 11, pp. 3685–3691, 2015.

[8] A. Serb *et al.*, "Unsupervised learning in probabilistic neural networks with multi-state metal-oxide memristive synapses," *Nature Communications*, vol. 7, p. 12611, sep 2016.

[9] S. G. Hu *et al.*, "Associative memory realized by a reconfigurable memristive Hopfield neural network," *Nature Communications*, vol. 6, p. 7522, jun 2015.

[10] S. Kvatinsky, M. Ramadan, E. G. Friedman, and A. Kolodny, "VTEAM: A General Model for Voltage-Controlled Memristors," *Circuits and Systems II: Express Briefs, IEEE Transactions on*, vol. 62, no. 8, pp. 786–790, 2015.

[11] C. Yakopcic, T. M. Taha, G. Subramanyam, and R. E. Pino, "Generalized memristive device SPICE model and its application in circuit design," *IEEE Transactions on Computer-Aided Design of Integrated Circuits and Systems*, vol. 32, no. 8, pp. 1201–1214, 2013.

[12] M. Laiho, E. Lehtonen, A. Russell, and P. Dudek, "Memristive synapses are becoming reality," *The Neuromorphic Engineer*, pp. 10–12, 2010.

[13] T. Chang *et al.*, "Synaptic behaviors and modeling of a metal oxide memristive device," *Applied Physics A: Materials Science and Processing*, vol. 102, no. 4, pp. 857–863, 2011.

[14] J. G. Simmons, "Generalized Formula for the Electric Tunnel Effect between Similar Electrodes Separated by a Thin Insulating Film," *Journal of Applied Physics*, vol. 34, no. 6, pp. 1793–1803, 1963.

[15] Z. Biolek, D. Biolek, and V. Biolková, "SPICE model of memristor with nonlinear dopant drift," *Radioengineering*, vol. 18, no. 2, pp. 210–214, 2009.

[16] T. Prodromakis, B. P. Peh, C. Papavassiliou, and C. Toumazou, "A versatile memristor model with nonlinear dopant kinetics," *IEEE Transactions on Electron Devices*, vol. 58, no. 9, pp. 3099–3105, 2011.

[17] S. Kvatinsky, E. G. Friedman, A. Kolodny, and U. C. Weiser, "TEAM: Threshold adaptive memristor model," *IEEE Transactions on Circuits and Systems I: Regular Papers*, vol. 60, no. 1, pp. 211–221, 2013.

[18] H. Li, P. Huang, B. Gao, B. Chen, X. Liu, and J. Kang, "A SPICE model of resistive random access memory for large-scale memory array simulation," *IEEE Electron Device Letters*, vol. 35, no. 2, pp. 211–213, 2014.

[19] Z. Jiang *et al.*, "A Compact model for metal-oxide resistive random access memory with experiment verification," *IEEE Transactions on Electron Devices*, vol. 63, no. 5, pp. 1884–1892, 2016.

[20] R. Berdan *et al.*, "A u-Controller-Based System for Interfacing Selectorless RRAM Crossbar Arrays," *IEEE Transactions on Electron Devices*, vol. 62, no. 7, pp. 2190–2196, 2015.

[21] Y.-F. Wang, Y.-C. Lin, I.-T. Wang, T.-P. Lin, and T.-H. Hou, "Characterization and Modeling of Nonfilamentary Ta/TaOx/TiO2/Ti Analog Synaptic Device," *Scientific Reports*, vol. 5, p. 10150, may 2015.

[22] K. Seo *et al.*, "Analog memory and spike-timing-dependent plasticity characteristics of a nanoscale titanium oxide bilayer resistive switching device," *Nanotechnology*, vol. 22, no. 25, p. 254023, 2011.

[23] C. Wang, W. He, Y. Tong, and R. Zhao, "Investigation and Manipulation of Different Analog Behaviors of Memristor as Electronic Synapse for Neuromorphic Applications," *Scientific Reports*, vol. 6, p. 22970, mar 2016.

[24] P. R. Mickel *et al.*, "A physical model of switching dynamics in tantalum oxide memristive devices," *Applied Physics Letters*, vol. 102, no. 22, 2013.

[25] S. H. Jo *et al.*, "Nanoscale memristor device as synapse in neuromorphic systems," *Nano Letters*, vol. 10, no. 4, pp. 1297–1301, 2010.

[26] U. Celano, *Filamentary-Based Resistive Switching*. Cham, Switzerland: Springer International Publishing, 2016, pp. 11–45.

[27] C.-W. Hsu *et al.*, "Homogeneous barrier modulation of TaO/TiO bilayers for ultra-high endurance three-dimensional storage-class memory," *Nanotechnology*, vol. 25, no. 16, p. 165202, 2014.

[28] F. Corinto and A. Ascoli, "A boundary condition-based approach to the modeling of memristor nanostructures," *IEEE Transactions on Circuits and Systems I: Regular Papers*, vol. 59, no. 11, pp. 2713–2726, 2012.

[29] I. Gupta *et al.*, "Real-time encoding and compression of neuronal spikes by metal-oxide memristors," *Nature Communications*, vol. 7, p. 12805, sep 2016.

[30] I. Messaris *et al.*, "A tio2 reram parameter extraction method," in *2017 IEEE International Symposium on Circuits and Systems (ISCAS)*, May 2017, pp. 1–4.

[31] D. Carta *et al.*, "Investigation of the switching mechanism in tio2-based rram: A two-dimensional edx approach," *ACS Applied Materials & Interfaces*, vol. 8, no. 30, pp. 19 605–19 611, 2016.

[32] Y. N. Joglekar and S. J. Wolf, "The elusive memristor: signatures in basic electrical circuits," *Physics*, pp. 1–22, 2008.

[33] "Eureqa, Nutonian," 2017. [Online]. Available: http://www.nutonian.com/

[34] I. Messaris *et al.*, "Live demonstration: A tio2 reram parameter extraction method," in *2017 IEEE International Symposium on Circuits and Systems (ISCAS)*, May 2017, pp. 1–1.

[35] Q. Li, A. Serb, T. Prodromakis, and H. Xu, "A memristor SPICE model accounting for synaptic activity dependence," *PLoS ONE*, vol. 10, no. 3, 2015.

[36] H. Abdalla and M. D. Pickett, "SPICE modeling of memristors," in *Proceedings - IEEE International Symposium on Circuits and Systems*, 2011, pp. 1832–1835.

[37] R. Berdan, C. Lim, A. Khiat, C. Papavassiliou, and T. Prodromakis, "A memristor SPICE model accounting for volatile characteristics of practical ReRAM," *IEEE Electron Device Letters*, vol. 35, no. 1, pp. 135–137, 2014.

[38] P. Y. Chen and S. Yu, "Compact Modeling of RRAM Devices and Its Applications in 1T1R and 1S1R Array Design," *IEEE Transactions on Electron Devices*, vol. 62, no. 12, pp. 4022–4028, 2015.

[39] S. Kvatinsky *et al.*, "Verilog-A for Memristor Models," *CCIT Technical Report*, vol. 8, no. December, 2011.

[40] D. Biolek, M. Di Ventra, and Y. V. Pershin, "Reliable SPICE simulations of memristors, memcapacitors and meminductors," *Radioengineering*, vol. 22, no. 4, pp. 945–968, 2013.

[41] I. Messaris, A. Serb, and T. Prodromakis, "Dataset for a computationally efficient verilog-a reram model (v.2)," May 2017. [Online]. Available: https://eprints.soton.ac.uk/411693/

[42] Accellera, "Verilog-AMS Language Reference Manual," p. 392, 2009.

[43] K. Szot *et al.*, "TiO2–a prototypical memristive material," *Nanotechnology*, vol. 22, no. 25, p. 254001, 2011.

Ioannis Messaris is a Phd student at the Physics dept., Aristotle University of Thessaloniki. His research interests are: transistor and memristor device modeling and CMOS digital cell modeling.

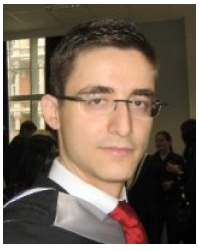

Alexander Serb (M11) is a research fellow at the Electronics and Computer Science (ECS) dept., University of Southampton, UK. His research interests are: instrumentation, algorithms and applications for RRAM testing, and neuro-inspired engineering.

Spyros Stathopoulos received his Diploma in Applied Physics and his MSc in Microelectronics and Nanodevices from the National Technical University of Athens (NTUA), Greece in 2009 and 2011 respectively. In 2015 he was awarded his PhD in Applied Physics from NTUA working on shallow junction engineering in silicon and germanium As of 2016 he is with the NanoGroup, School of Electronics and Computer Science, University of Southampton, UK working on the fabrication and characterization of memristive devices.

Ali Khiat is an Experimental Officer at Southampton Nanofabrication Centre, University of Southampton. His current main research interests are micro-/nanofabrication, optimisation, metrology and characterization of memristors and memristive devices.

Nikolaidis Spyridon (SM88) is a full professor at the Physics dept., Aristotle University of Thessaloniki. His current research interests include: modeling the operations of basic CMOS structures, development of analytical expressions for the propagation delay and the power consumption of logic gates, design of high speed and low power digital circuit and embedded systems, modeling the power consumption of embedded processors.

Themistoklis Prodromakis (SM08) is a Professor of Nanotechnology and EPSRC and Royal Society Industry Fellow affiliated with the Southampton Nanofabrication Centre at the University of Southampton. He previously held a Corrigan Fellowship in Nanoscale Technology and Science within the Centre for Bio-inspired Technology at Imperial College and a Lindemann Trust Visiting Fellowship in EECS UC Berkeley. Prof Prodromakis is a Fellow of the IET, Fellow of the Institute of Physics, Senior Member of the IEEE. His background is in Electron Devices and nanofabrication techniques, with his research being focused on bio-inspired devices for advanced computing architectures and biomedical applications..